Supporting Information

Sulphur Vacancy driven phase conversion of MoS_2 nanosheet for efficient photoreduction of CO_2 under visible light

Kousik Das,[a] Sarika Lohkna,[b] Gang Yang,[c] Prasenjit Ghosh[†b, d] and Soumyajit Roy[*a]

[a]Department of Chemical Sciences, Indian Institute of Science Education and Research, Mohanpur 741246, Kolkata, India.
[b]Department of Chemistry, Indian Institute of Science Education and Research (IISER), Pune 411008, India.
[c]Department of Chemistry, Changshu Institute of Technology, Changshu, P. R. China.
[d]Department of Physics, Indian Institute of Science Education and Research (IISER), Pune 411008, India.

Experimental Section

Materials:

All chemicals and solvents were used as obtained unless otherwise noted. Hexaammonium Heptamolybdate Tetrahydrate ($(NH_4)_6Mo_7O_{24}.4H_2O$), Polyacrylonitrile (PAN), Thiourea (CH_4N_2S), Sodium Hydroxide (NaOH) were obtained from Alfa Aesar. 5,5-Dimethyl-1-pyrroline N-oxide (DMPO), Poly(ethylene glycol) Ethyl Ether (Ethoxypolyethylene Glycol) were purchased from Sigma-Aldrich. High purity $^{13}CO_2$ (99.0 atom %) was acquired from Sigma-Aldrich.

Characterization:

Electronic absorption spectra were recorded on a U-4100 spectrophotometer from 200 cm^{-1} to 1000 cm^{-1}. A Jasco V-670 spectrophotometer was used for UV-Vis diffuse reflectance spectroscopy (DRS). $BaSO_4$ was used as a standard sample for 100% reflectance. The obtained UV-vis diffuse reflectance spectra were first transformed into absorption spectra according to the Kubelka-Munk function,

$$F(R) = \frac{(1-R)^2}{2R} \times 100\%$$

where R was the relative reflectance of samples with infinite thickness compared to the reference. The band gaps of the samples were then estimated based on the Tauc equation,

$$F(R)h\nu = A\left(h\nu - E_g\right)^{\frac{n}{2}}$$

where, h, ν, A, and E_g represent Planck constant, incident light frequency, proportionality constant and band gap, respectively, while n depends on the nature of transition in a semiconductor. Values of 1, 3, 4, and 6 for n correspond to allowed direct, forbidden direct, allowed indirect, and forbidden indirect transitions, respectively. The value of E_g was then determined from the plot of $(F(R)h\nu)^{2/n}$ versus $h\nu$ and corresponded to the intercept of the extrapolated linear portion of the plot near the band edge with the $h\nu$ axis. Because the exfoliated MoS_2 nanosheet is a direct bandgap material, the E_g value was obtained by plotting $(F(R)h\nu)^2$ versus $h\nu$. A JEOL JEM 2010 electron microscope was used for TEM imaging. Dispersions of MoS_2 nanosheets were drop casted over a carbon-coated copper grid and dried under a high vacuum before doing the microscopic analysis. A SUPRA 55 VP-41-32 scanning electron microscope fitted with smart-SEM version 5.05 software was used for SEM imaging. Sample preparation was done by drop-casting the dispersion of MoS_2 nanosheets over a silicon wafer and dried under a vacuum in a dust-free area. The XRD patterns were obtained by using a Rigaku instrument (Mini Flex II, Japan), by using Cu Kα radiation with an incident wavelength of 1.5406 Å operating under a voltage of 30 kV and a current of 50 mA. The scan rate was 3° min^{-1}. FT-IR spectra were

recorded by Perkin Elmer spectrum Rx1 Spectrophotometer. In each case, 1 mg of the sample was mixed with dry KBr, and a pellet was prepared from the mixture. The spectra were recorded in the range of 400-4000 cm^{-1}. Raman measurements were carried out over the wavenumbers range of 100-900 cm^{-1} using micro-Raman spectrometer LABRAM HR from Horiba Jobin Yvon. The TGA experiments were carried out on a Mettler Toledo TGA/SDTA851e instrument. The heating rate was 10°C/minute. Fluorescence measurements were performed in HORIBA Fluoromax PLUS R928P. Each time 3 ml sample solution was taken in a quartz cuvette for fluorescence experiment. For the measurement of 2-OHterephthalic acid, the excitation wavelength was set to 315 nm and emission was detected in the range of 325 nm to 610 nm with a 5 nm bandpass. Atomic force microscopy (AFM) measurements were carried out with a Nasoscope model Multimode 8 Scanning Probe Microscope to analyze the thickness of the samples. Time-resolved photoluminescence (TRPL) and lifetime measurement has been carried out by using FLS 1000 Edinburgh instrument. X-ray absorption spectroscopy (XAS) was performed at PETRA III, P64 beamline. DESY, Germany. Measurements were conducted under ambient conditions for Mo K-edge in the transmission mode. ICP-OES analysis was performed in Perkin Elmer Optima 7000 DV instrument. ^{1}H NMR was recorded at 400 MHz and the spectra were further enhanced by solvent suppression technique. Chemical shifts (δ) are reported in ppm and the intensity of the peaks was measured using phenol as an internal standard. CO_2-reduced products were quantified using a Trace 1300 GC and ISQ QD single quadrupole GC-MS system. For the analysis of formic acid, it was first esterified with ethanol to form ethyl formate in a headspace vial. This ethyl formate was taken for GC-MS analysis. A five-point calibration curve was drawn using a known concentration of formic acid under the same external condition. From this calibration curve, the yield of formic acid from CO_2 reduction was calculated. XPS spectra were acquired on a Thermo Fisher Scientific Instrument with Al Kα as the excitation source. The binding energies obtained in the XPS spectral analysis were corrected by referencing C 1s to 284.8 eV. *In situ* Diffuse Reflectance Infrared Fourier Transform Spectroscopy (DRIFTS) was performed using a purged VERTEX FT-IR spectrometer equipped with the A530/P accessory and a mid-band Mercury Cadmium Telluride (MCT) detector. A DRIFTS cell with a quartz window was used to perform the catalytic experiment. Each spectrum was recorded after 100 scans with a resolution of 4 cm^{-1}. 20mg of the sample was kept in the DRIFTS cell and purged with N_2 for 30 min to remove air from the cell. Then CO_2 and water vapor mixture were injected into the cell and light was illuminated through the quartz window. First data was collected just before the light exposure and after that data were collected after 15-minute intervals. A CHI400A potentiostat with a three-electrode configuration under the illumination of blue LED light was used for photoelectrochemical experiments. For all the experiments, a saturated Calomel electrode (Hg/Hg_2Cl_2) was used as the reference, and Pt wire was used as the counter in 0.5M Na_2SO_4 aqueous solution.

Synthesis of MoS_2/carbon nanofiber composite:

The carbon nanofibers were synthesized by electrospinning and carbonization following a previously reported synthesis.[1] In a typical procedure, polyacrylonitrile (PAN) was dissolved in N, N-dimethylformamide (DMF) at 70°C, and then the mixture was stirred for 12 hours at room temperature to obtain a homogeneous solution. By employing high voltage electrospinning of 14 kV, a white film was collected from an aluminum foil. The substrate was then pre-oxidation at 270°C for 3 h under an air atmosphere and finally carbonized at 750°C for 3 h under an N_2 atmosphere to produce black carbon nanofiber films.

Bulk MoS_2 material was synthesized using the following procedure. 0.100 g of thiourea (CH_4N_2S), 0.29 g of sodium hydroxide (NaOH), and 0.25 g of hexaammonium heptamolybdate tetrahydrate ($(NH_4)_6Mo_7O_{24}.4H_2O$) were dissolved in 80 mL deionized water. The solution was transferred into a 100 mL Teflon-lined stainless-steel autoclave, meanwhile, carbon nanofibers film was also added into the autoclave as the source of carbon nanofiber (CNF). After hydrothermal reaction at 200°C for 12 h, the as-produced CNF-MoS_2 sample was washed with distilled water and absolute ethanol repeatedly to

remove the unreacted compounds. The sample was then dried at 70 °C for 12 h. The final black material was denoted as bulk MoS_2 and used as the starting material for our experiments.

Exfoliation of MoS_2 nanosheets:

2 mg of bulk MoS_2 was taken in 10 mL of distilled water in a reaction vial. Bulk MoS_2 was suspended properly in water before adding the surfactant solution. In a separate reaction vial, a 20% w/w ratio solution of ethoxypolyethylene glycol was prepared in distilled water. The surfactant solution was then added slowly (0.01 mL/min) to the MoS_2 dispersion over 10 hours. A few mL solutions were taken intermittently for UV-Vis measurements. After sonication, the dispersion was centrifuged at 5000 rpm for 10 mins. The supernatant was discarded to remove the excess surfactant and the sediment was subsequently redispersed in water to prepare the final solution. The final exfoliated solution was then used for additional experiments.

The analysis of decomposition of H_2O_2 by S vacancy:

The S vacancy present in the sample was used for the decomposition of H_2O_2 to produce ·OH. The amount of hydroxyl radical was measured from the fluorescence intensity of 2-hydroxyterephthalic acid resulting from the reaction of ·OH with terephthalic acid. To do this experiment, a 2 ml solution containing 50 mM H_2O_2 and 6 mM terephthalic acid was added to a 5 ml solution of MoS_2 (0.2 mg/ml). The mixture was then irradiated with blue LED light for 1 hour. The reacted solution was centrifuged to remove the MoS_2 sheets and the centrifuged sample was used for the Fluorescence analysis. The fluorescence intensity of the generated 2-hydroxyterephthalic acid was recorded at 426 nm after excitation at 315 nm.

Photocatalytic CO_2 reduction:

A 10 mL solution of surfactant-exfoliated MoS_2 nanosheets was taken in a quartz glass vial. Pure CO_2 was bubbled through the solution until saturation to remove the dissolved air and saturate the solution with CO_2. The reaction vial was then properly sealed and kept in a blue-LED lit chamber. The light flux measured ranged from 0.12 to 0.10 W/cm^2 (at 475 nm). Small aliquots of liquid samples and gas samples were taken during the experiment for NMR and GC-MS analysis, respectively.

Photocatalytic degradation of methylene blue:

To investigate the hole-mediated ·OH formation from the oxidation of water during photocatalysis, a dye degradation reaction was performed. In a typical experiment, a dilute aqueous solution of methylene blue was added to a 10 ml dispersion of exfoliated MoS_2 (0.2 mg/ml) in water. The mixture was irradiated with blue LED light for 3 hours. A small aliquot was taken intermittently for the UV-Vis experiment. For the study of the hole and ·OH scavenger, sodium acetate, and t-butyl alcohol were added before starting the dye degradation reaction.

Apparent quantum yield (AQY) calculation

After 14 hours of CO_2 reduction, the AQY was calculated using the following equation:

$$AQY(\%) = \frac{Number\ of\ reacted\ electrons}{Number\ of\ incident\ photons} X100\%$$

The number of reacted electrons was calculated from the yield of CO_2-reduced products and HER-

$$CO_2(g) + 2H^+ + 2e^- = HCOOH(g)$$

$$CO_2(g) + 6H^+ + 6e^- = CH_3OH(g) + H_2O(l)$$

$$2H^+ + 2e^- = H_2(g)$$

Because different numbers of electrons are required for the formation of different products, the total number of reacted electrons are

$$Number\ of\ reacted\ electrons = \left[2n(H_2) + 6n(CH_3OH) + 2n(HCOOH)\right]XN_A$$

where, n(H_2), n(CH_3OH), and n(HCOOH) are the yields of hydrogen, methanol, and formic acid in moles, respectively. N_A is Avogadro's number.

The number of incident photons is calculated from the following equation:

$$Number\ of\ incident\ photons = \frac{PS\lambda t}{hc}$$

where, P is the power density of the incident monochromatic light (W/m^2), S (m^2) is the irradiation area, t (s) is the duration of the incident light exposure and λ (m) is the wavelength of the incident monochromatic light.

Combining these two equations the AQY(%) for different monochromatic light was calculated. For example, the AQY(%)@475 nm is shown here-

AQY(%)@475 nm

$$\frac{\left[(21.6 \times 2 + 9.9 \times 6 + 3.9 \times 2) \times 10^{-6}\right] \times 6.02 \times 10^{23}}{1} \times \frac{6.626 \times 10^{-34} \times 3 \times 10^{8}}{100 \times 10^{-3} \times 2.54 \times 475 \times 10^{-9} \times 3600 \times 14} \times 100\%$$

$$= 0.22\%$$

Computational Methods

All the calculations have been done using the plane wave based DFT suite of the Quantum ESPRESSO package (version 6.5).[2] The Perdew-Burke-Ernzerhof (PBE) parametrization of the generalised gradient approximation (GGA) has been used to describe the exchange correlation functional.[3] Semi-empirical 'Grimme's correction has been used to account for the Van der Waals interactions. Ultrasoft pseudopotentials have been used to describe the electron-ion interactions.[4] The following valence configurations for different elements are considered in the calculations: (a) Mo ($4s^2$, $4p^6$, $4d^4$, $5s^2$), (b) S ($3s^2$, $3p^4$), (c) C ($2s^2$, $2p^2$), (d) O ($2s^2$, $2p^4$) and (e) H ($1s^1$). The wavefunctions are expanded in a plane wave basis set whose size is determined by kinetic energy cut off of 50 Ry (500 Ry) for wavefunction (charge density). 2H, 1T, and 1T′ phases of MoS_2 have been considered and monolayers have been generated by adding 10 Å vacuum along the direction normal to the surface. For the primitive unit cells, Γ-centered 12 × 12 × 1 (for 2H and 1T phases) and 12 × 6 × 1 (for 1T′ phase) Monkhorst-Pack k-point grid are chosen while only Γ-point Brillouin zone integrations are done for gas phase molecules.[5] Gaussian smearing with 0.005 Ry smearing width has been used to achieve faster convergence of electronic energy. Spin-polarized calculations are done and the ground state is found to be nonmagnetic for each pristine surface.

In order to create S vacancies, supercells of different sizes are constructed to get different concentrations of S vacancies. The S vacancy concentration within a supercell is given as:

$$\%S\ vacancy = (n \times 100)/N \quad (1)$$

where n is the number of S atoms missing and N is the total number of MoS_2 units in a supercell. S vacancies are created in 3×3×1 and 4×4×1 supercells by removing one S atom from the top layer which results in 11.11% and 6.25% vacancy concentrations, respectively. The defect formation energies (E_{form}) per S vacancy have been calculated using the formula:

$$E_{form} = \left(E_{defect} - E_{prist} + X * \left(E_{S_8}/8\right)\right)/X \quad (2)$$

where E_{defect} and E_{prist} are the DFT energies of the structures with vacancies and corresponding supercell for the pristine phase respectively. E_{S_8} is the DFT energy of S_8 molecule in the gas phase and *X* denotes the number of S vacancies.

To incorporate the zero-point energy corrections we have computed the vibrational frequencies of the reactants, products and intermediates using the density functional perturbation theory.[6-8]

Elementary steps for such reaction involves simultaneous electron-proton transfer steps that can be represented as shown below:

$$A + e^- + H^+ \rightarrow B$$

In order to compute the free energy change for such a reaction, one needs to compute the free energy of an electron and a proton, which is computationally difficult. Hence to circumvent this problem, we have used the concept of computational hydrogen electrode proposed by Norskov according to which an electron and a proton is in equilibrium with gaseous H_2 at 0 V *vs* reversible hydrogen electrode i.e.,[9]

$$e^- + H^+ \rightleftharpoons \frac{1}{2}H_2$$

With this approximation the Gibbs free energy of an e^- and a H^+ will be equal to half the Gibbs free energy (G) of a H_2 molecule in gas phase.

$$G(e^-) + G(H^+) \rightleftharpoons \frac{1}{2}G(H_2)$$

From thermodynamics, the Gibbs free energy of a closed system is given by:[10]

$$G = H - TS = U + PV - TS,$$

Where *H*, *S*, and *U* denotes enthalpy, entropy and internal energy of the system while *P*, *V* and *T* represents pressure, volume and temperature. Since the DFT calculations are done at zero Kelvin, the corrections to *H* at finite temperatures is given by $\int_0^T C_p(T')dT'$, where C_p is the heat capacity at constant pressure. The internal energy is given by the sum of the DFT energy and the zero point energy (*ZPE*). Thus the equation for G becomes:

$$G = E_{DFT} + ZPE + \int_0^T C_p(T')dT' - TS$$

For gas phase molecules, all degrees of freedom (dof) contribute significantly. One can explicitly calculate these quantities using statistical mechanics or can use standard gas phase thermodynamic data available. To compute *G* for gas phase molecules, we have used gas phase entropy (S) and heat capacity (C_p) data at 298.15 K and 1 bar pressure, which is available in the NIST database.

During the reaction steps, water is also formed and it is in liquid form. However, computing the Gibbs free energy of liquid water ($G_{H_2O(l)}$) is difficult. Hence, to estimate $G_{H_2O(l)}$, we assume that water vapour is in equilibrium with liquid water and under this assumption $G_{H_2O(l)}$ can be written as:

$$G_{H_2O(l)} = G_{H_2O(g)} + RTln(P/P^o)$$

where, $G_{H_2O(g)}$ is the free energy of water under ideal gas approximation, R is the ideal gas constant, P is the vapor pressure of water at room temperature and P^o is the standard pressure, 1 bar. At 298.15 K, the temperature of interest, P=0.035 bar. Using this we can make reasonable estimates of the free energy of liquid water.

For solids (e.g. surfaces and species adsorbed on the surfaces), translational and rotational dof becomes less significant while contributions from vibrational dof can be incorporated using statistical mechanics as explained below. The Gibbs free energy for solids can be written as:

$$G_{solids} = E_{DFT} + ZPE - H_{vib} + TS_{vib}$$

where H_{vib} and S_{vib} are the enthalpic and entropic contributions by vibrational dof. Vibrational partition function (q_{vib}) have been calculated from the vibrational frequencies (ν_i), which we have computed within the harmonic approximation. H_{vib} and S_{vib} have been calculated from q_{vib} using following equations:

$$q_{vib} = \prod_i q_{vib_i} = \prod_i \frac{1}{1 - exp\left(\frac{-\Theta_{vib_i}}{T}\right)}$$

$$S_{vib} = \left[\sum_i ln\left(\frac{1}{1 - exp\left(\frac{-\Theta_{vib_i}}{T}\right)}\right) + \sum_i \frac{\Theta_{vib_i}}{T} \frac{1}{exp\left(\frac{-\Theta_{vib_i}}{T}\right) - 1}\right]$$

$$H_{vib} = k_B\left[\sum_i \Theta_{vib_i} \frac{1}{exp\left(\frac{\Theta_{vib_i}}{T}\right) - 1}\right]$$

where $\Theta_{vib_i} = h\nu_i/k_B$, h and k_B are Planks's constant and Boltzmann constant respectively.

Tables

Table S1. Ratio of the S and Mo atoms calculated from the XPS spectra

Sample	Element	Atomic %	Ratio	S vacancy/MoS_2
Bulk MoS_2	S	66.1	1.95	0.05
	Mo	33.9		
Exfoliated MoS_2	S	64.5	1.87	0.13
	Mo	34.5		

Table S2. The stoichiometric ratio of Mo and S obtained from ICP-OES

Sample	Weight% of Mo	Weight% of S	Stoichiometric ratio of Mo:S	S vacancy/MoS_2
Bulk MoS_2	60.19	38.85	1:1.93	0.07

Exfoliated MoS_2	61.72	37.95	1:1.84	0.16

Table S3. Fitting results of the Mo K-edge EXAFS spectra of bulk and exfoliated MoS_2.

Sample	Shell	Coordination Number	Bond length (Å)	ΔE_0 (eV)	σ^2	Goodness of fit
Mo foil	Mo-Mo	8.0	2.72	5.239	0.004	0.006
	Mo-Mo	6.1	3.15		0.005	
Bulk MoS_2	Mo-S	5.8	2.39	0.438	0.001	0.007
	Mo-Mo	5.6	3.15		0	
Exfoliated MoS_2	Mo-S	5.3	2.41	1.414	0.001	0.009
	Mo-Mo	4.8	2.97		0.003	

Table S4. Calculated lattice parameters, bond lengths, and band gap for 2H, 1T, and 1T′ monolayers. E_{rel} is the energy of the different phases with respect to the most stable 2H phase.

Properties	**2H Phase**			**1T Phase**			**1T′ Phase**		
	Calc. (This work)	Theor.[11]	Exp.[15]	Calc. (This work)	Theor.[12-14]	Exp.	Calc. (This work)	Theor.[12-14]	Exp.[16]
E_{rel} (eV/fu)	0.00	-	-	0.83	0.83 0.85	-	0.59	0.54 0.51	-
a (Å)	3.19	3.19	-	3.20	3.18 3.19	-	3.19	3.17	3.18
b (Å)	-	-	-	-	-	-	6.50	6.54	6.55
Mo-Mo (Å)	3.19	3.18	-	3.20	3.18	-	3.18, 2.78, 3.75	3.17, 2.77, 3.80	-
Mo-S (Å)	2.41	2.41	-	2.43	2.43	-	2.39- 2.50	2.39-2.51	-
Thickness (Å)	3.12	3.13	-	3.15	3.18	-	3.07	-	-
Band gap (eV)	1.66	1.67	1.90	-	-	-	0.007	0.006	-

Table S5. Defect formation energies for S vacancies in 2H, 1T, and 1T′ phases with respect to the corresponding pristine phase. The numbers in parentheses are the defect formation energies with respect to the 2H phase without any S vacancy.

S vacancy conc.	**E_{form} (eV)**		
	2H Phase	**1T Phase**	**1T′ Phase**
6.25 %	2.93 (2.93)	-0.14 (13.08)	-1.78 (11.44)
11.11 %	2.95 (2.95)	-0.60 (6.84)	-

Table S6. Comparison of MoS_2 based photocatalytic CO_2 reduction to methanol.

Catalyst	**Reaction conditions**	**CO_2-reduced product(s)**	**Methanol production (μmol g^{-1} h^{-1})**	**References**
MoS_2 (2H-1T′)	2.5 mg in 10 ml DI water, 100 mW/cm^2 blue LED light	CH_3OH, HCOOH	9.9	**This work**
MoS_2 (2H)/ TiO_2 hybrid nanosheets	0.1 g catalyst, 1 M $NaHCO_3$ solution, 300W xenon arc lamp	CH_3OH, C_2H_5OH and CH_3CHO	10.6	[17]*Nanoscale*, **2017**, 9, 9065
α-Fe_2O_3/MoS_2 (1T)	50 mg in 5 ml DI water, 300W xenon lamp	CH_3OH, CH_4	41	[18]*ACS Sustain. Chem. Eng.*, **2020**, 8, 12603
MoS_2 (2H)/Bi_2WO_6	50 mg in 50 ml water, 300W xenon lamp	CH_3OH CH_3CH_2OH	9	[19]*Appl. Surf. Sci.*, **2017**, *403*, 230
MoS_2 (2H)/$Mn_{0.2}Cd_{0.8}S$	50 mg in 100 ml 0.1 M NaOH, 300 W xenon lamp	CH_3OH	2.13	[20]*New J. Chem.*, **2020**, 44, 13728-13737
Ag/MoS_2 (1T-2H)	0.02 g in 20 ml isopropanol, 250 W Hg lamp	CH_3OH	365	[21]*Energy Technol.*, **2019**, *7*, 1900582
MoS_2 (2H)/TiO_2	50 mg in 10 ml water, 350W xenon lamp	CH_4 CH_3OH	2.55	[22]*Adv. Optical Mater.* **2018**, 6, 1800911
ZnO/MoS_2 (2H)	100 mg in 50 ml 0.5 M $NaHCO_3$ solution, 150W xenon lamp	CH_3OH CH_3CHO	42.63	[23]*J. Environ. Chem. Eng.* **2022**, 10, 107337
MoS_2 (2H)/g-C_3N_4	50 mg in 100 ml water, 300W xenon lamp	CO	0	[24]*Dalton Trans.*, **2018**, 47, 15155
MoS_2 (2H)/Bi_2S_3	0.2 g in 40 ml DI water, 150 mW/cm^2 light	CO CH_4	0	[25]*Catalysts,* **2019***,* 9, 998

Table S7. Estimation of S vacancy from the peak intensity of EPR and fluorescence during the reaction

Reaction time (hours)	**EPR intensity (a.u.)**	**Estimated S vacancy from EPR (%)**	**Fluorescence intensity (a.u.)**	**Estimated S vacancy from fluorescence (%)**

0	707577	100	755	100
2	648446	92	716	95
4	509316	72	558	74
6	393044	56	400	53
10	329440	47	335	44
14	-	-	317	42

Figures

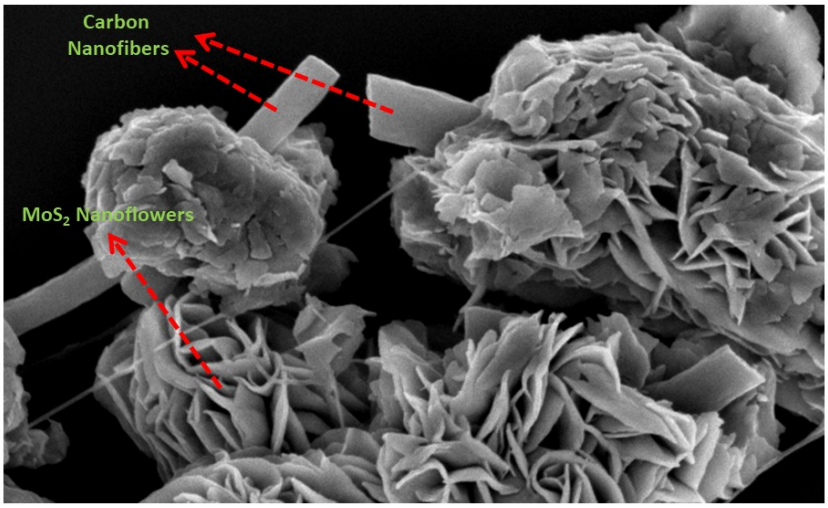

Figure S1. SEM image of the bulk sample containing MoS_2 nanoflowers and carbon nanofibers.

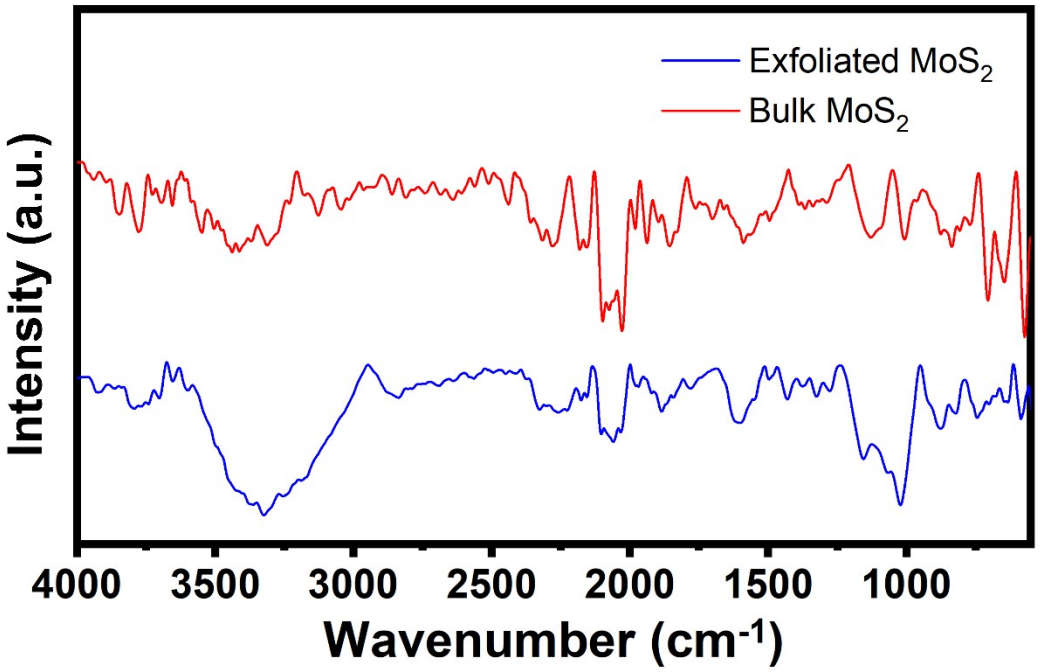

Figure S2. Comparison of ATIR spectra of the bulk and exfoliated MoS_2.

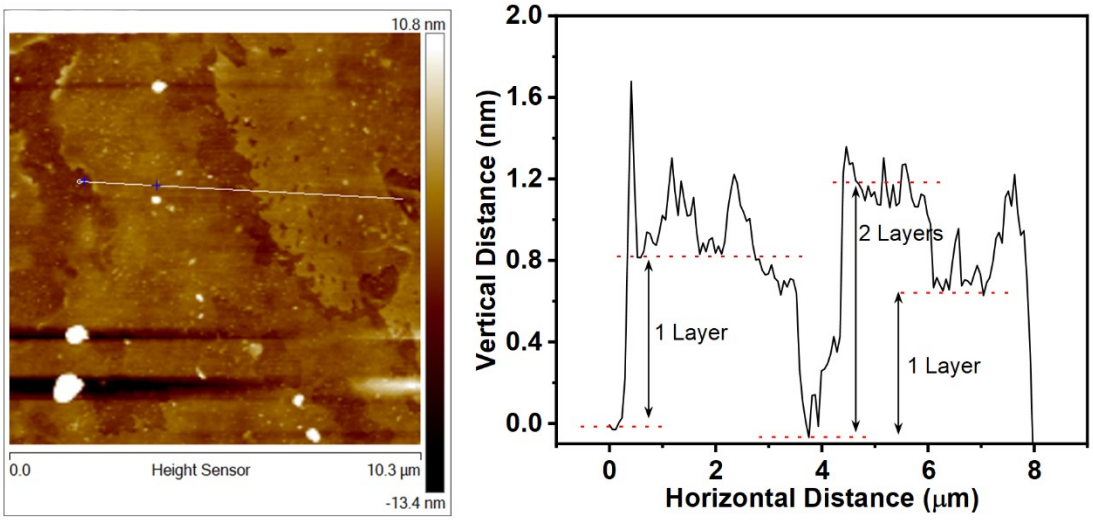

Figure S3. a) AFM image and b) the corresponding layer numbers of the exfoliated MoS_2 nanosheet.

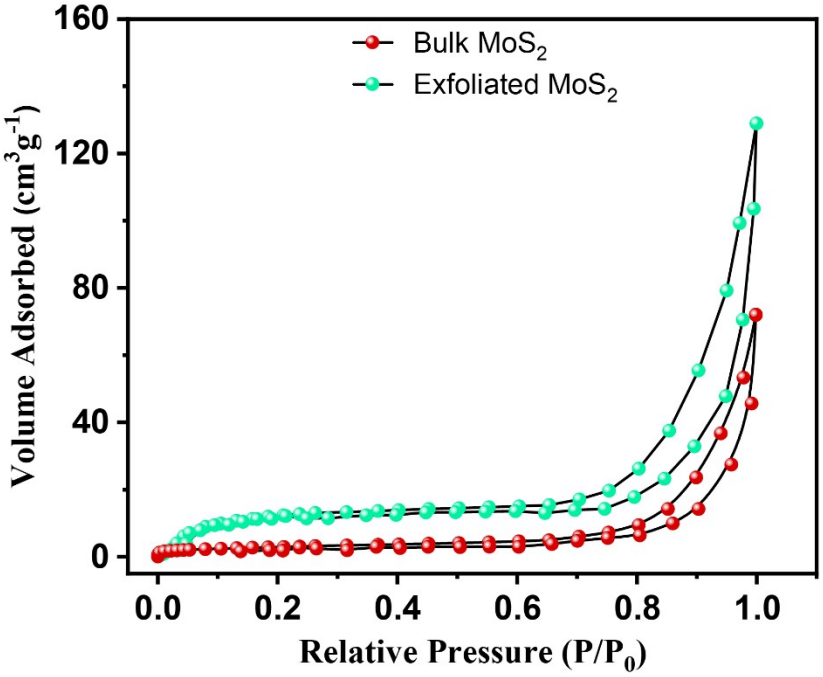

Figure S4. N_2 adsorption and desorption isotherms of bulk and exfoliated MoS_2. The surface area was determined by the Brunauer-Emmett-Teller (BET) (type IV isotherm).

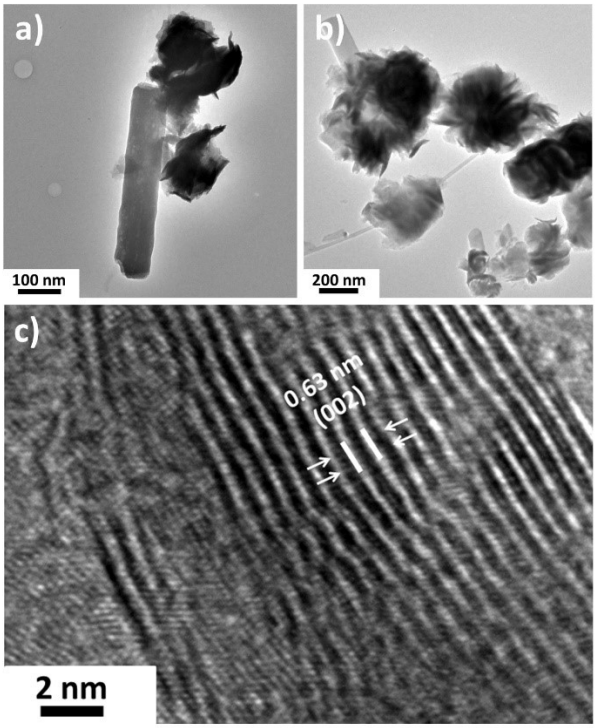

Figure S5. a) and b) TEM images of the bulk MoS_2 nanosheets. c) HRTEM image of the bulk MoS_2 showing the d-spacing of (002) plane to be 0.63 nm.

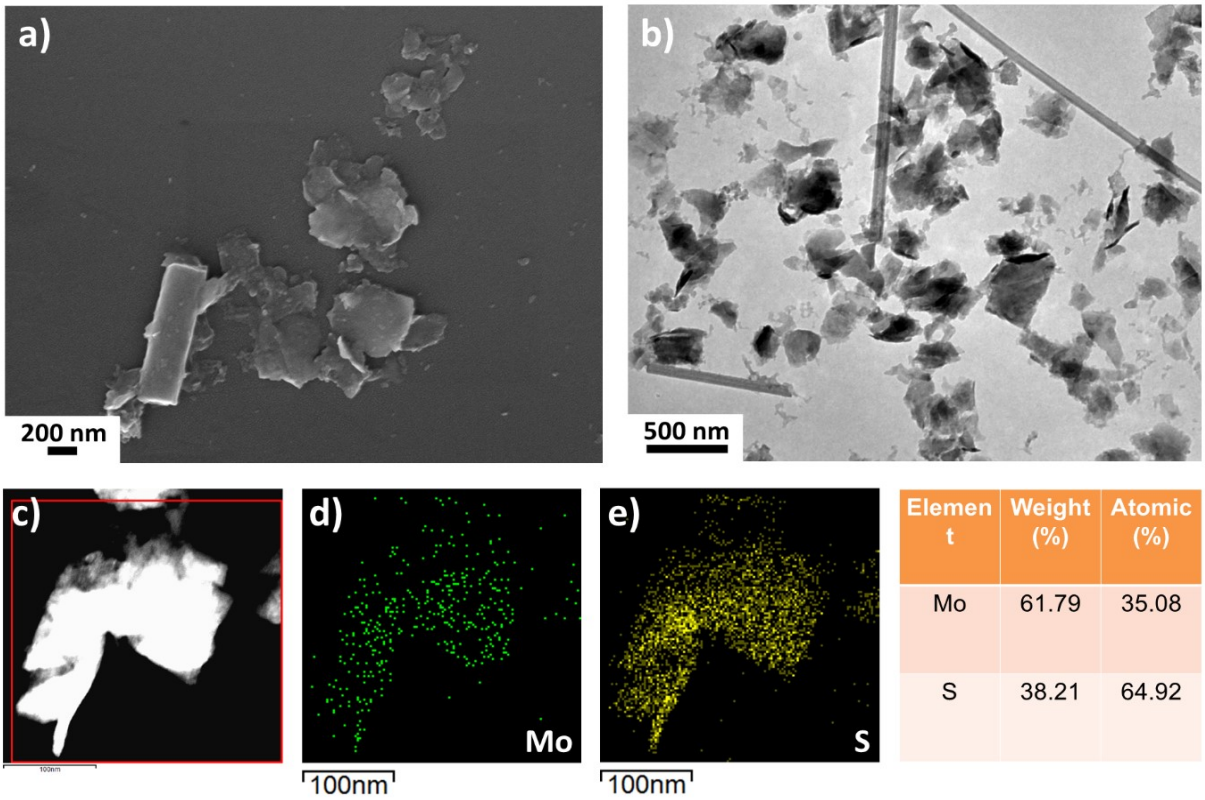

Element	Weight (%)	Atomic (%)
Mo	61.79	35.08
S	38.21	64.92

Figure S6. a) SEM and b) TEM image of the exfoliated MoS_2 nanosheets. c) STEM image of the exfoliated nanosheet. d) and e) EDAX mapping of Mo and S, respectively and their corresponding elemental percentage.

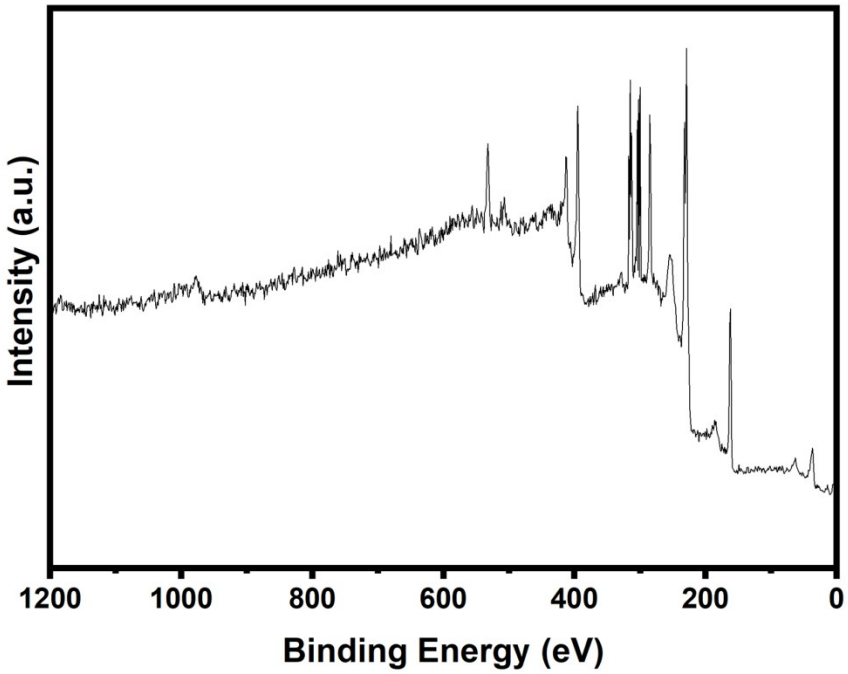

Figure S7. XPS survey spectrum of exfoliated MoS_2 nanosheets.

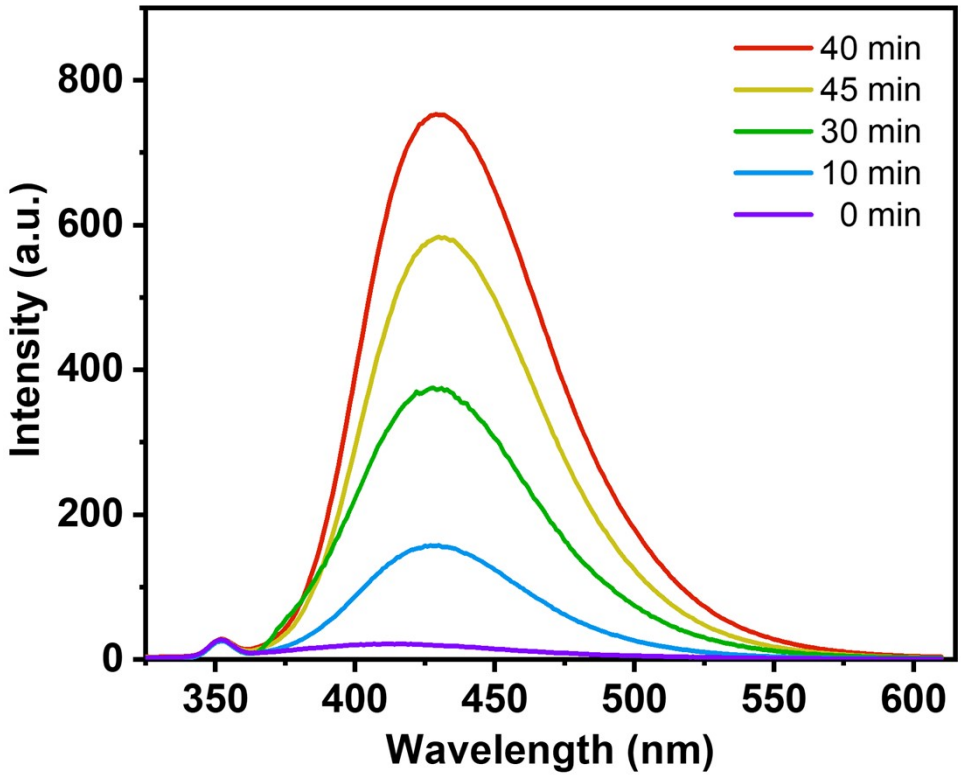

Figure S8. Time dependent fluorescence of 2-OHterephthalic acid produced from the reaction of terephthalic acid and H_2O_2 dissociated ·OH in S vacancy. Excitation wavelength was set to 315 nm.

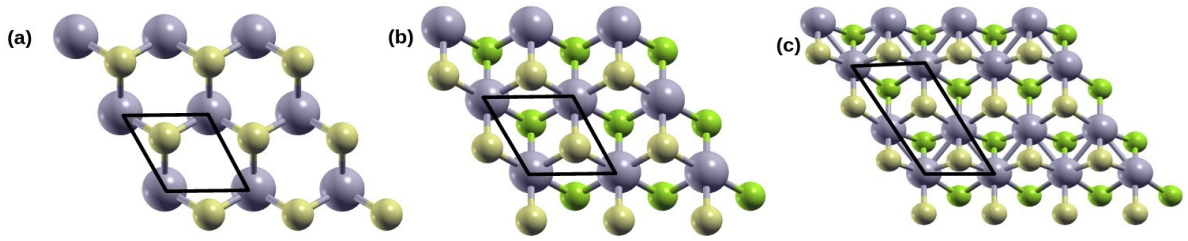

Figure S9. Optimized structures of a) 2H, b) 1T and c) 1T′ monolayers. Grey spheres represent Mo atoms, yellow and green spheres represent S atoms in top and bottom layers respectively. The unit-cell for each case is marked by black parallelogram.

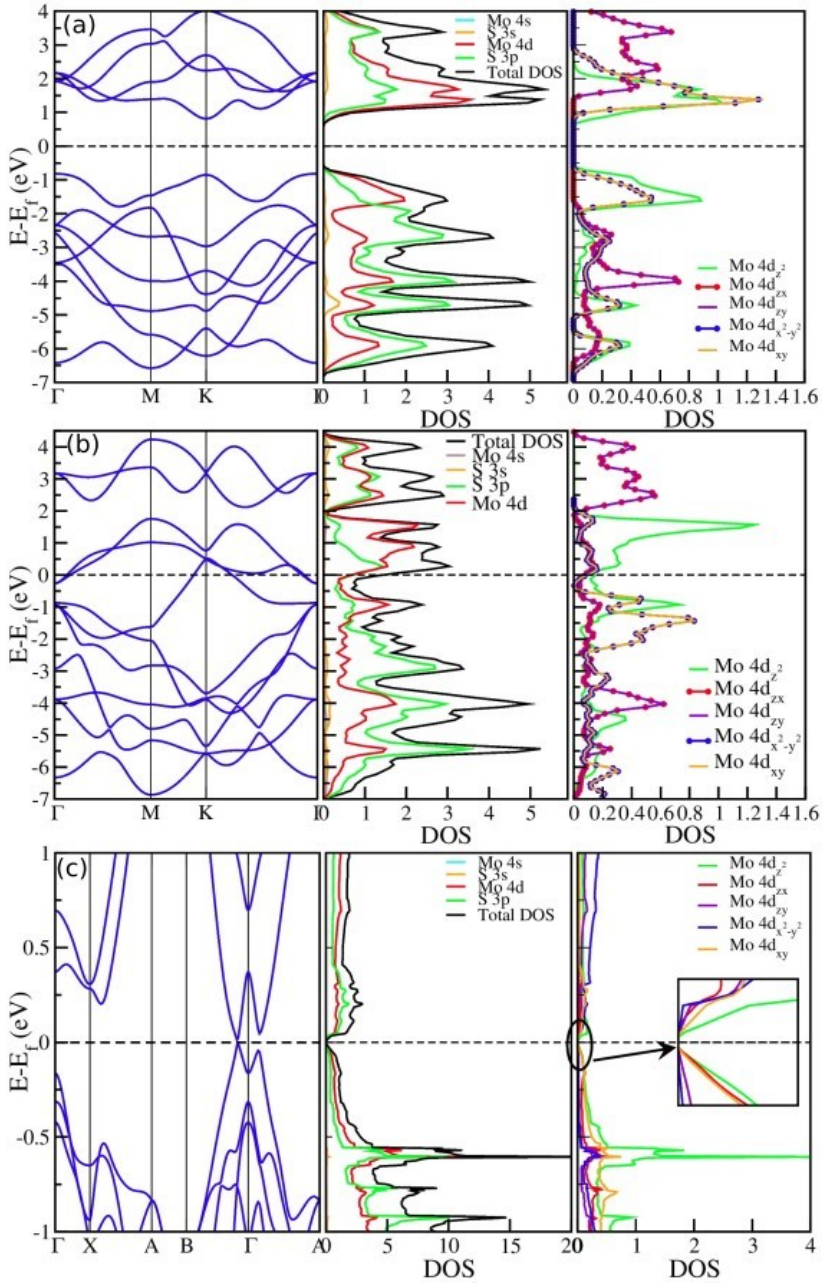

Figure S10. Electronic structure of pristine monolayers: band structure (left) density of states projected on atomic orbitals (middle) and density of states projected on Mo d orbitals (right) for (a) pristine 2H (b) 1T and (c) 1T′ phase.

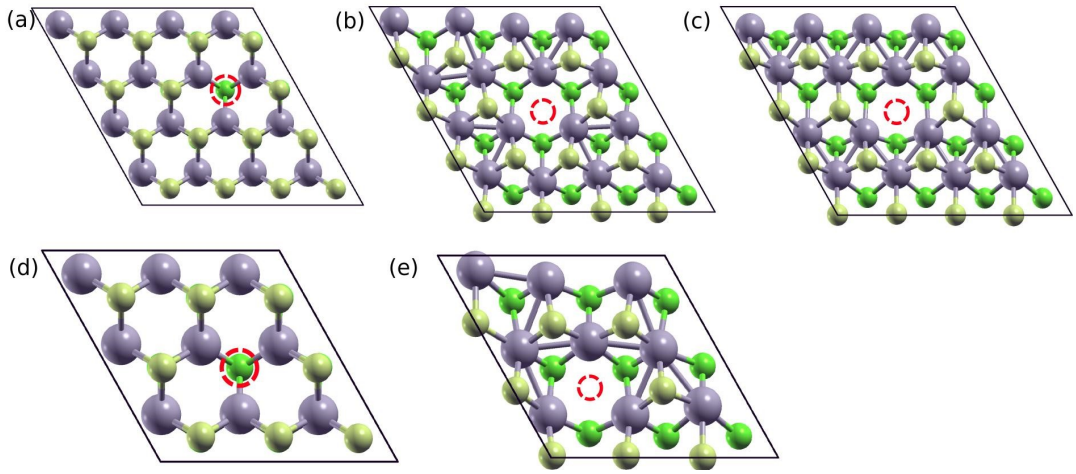

Figure S11. Optimized structures of S vacancies in different phases: 6.25% S vacancy in a) 2H, (b) 1T, (c) 1T′ phase and 11.11% isolated and 11.11% S vacancy in d) 2H, (e) 1T phase (structure with 11.11% S vacancy in 1T′ phase is not obtained). Grey spheres represent Mo atoms, Yellow and green spheres represent S atoms in top and bottom layers respectively. Vacancy sites are represented by red circles.

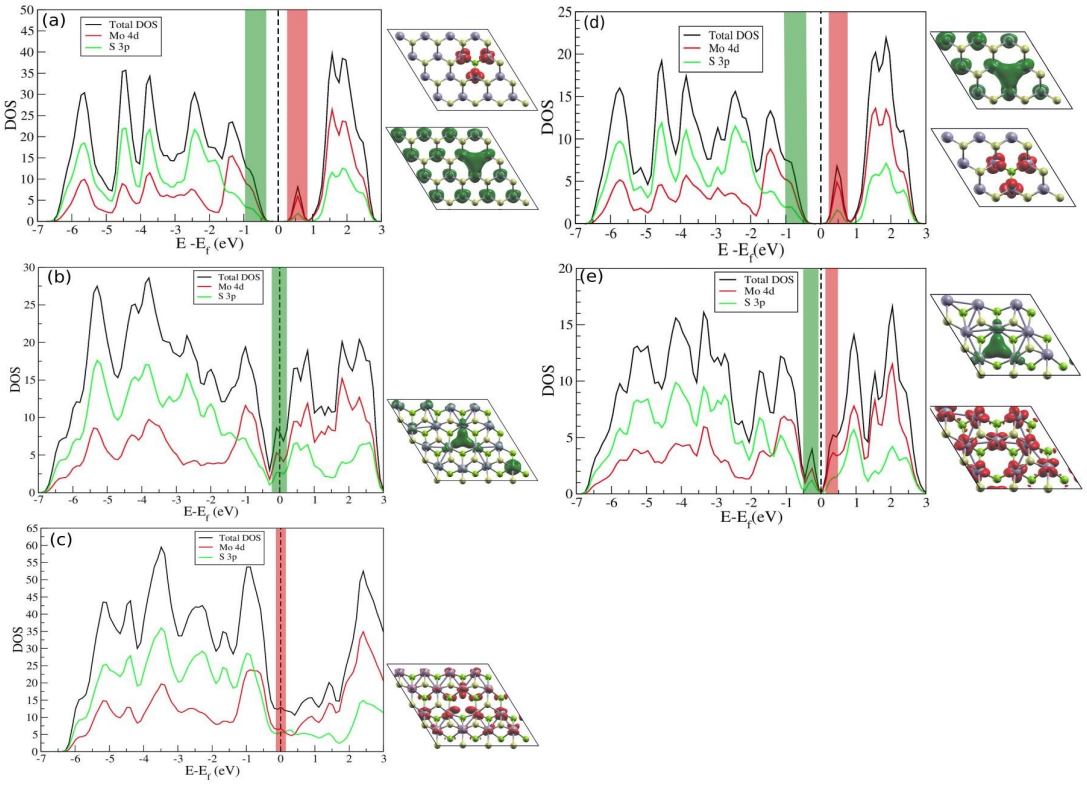

Figure S12. Projected density of states (PDOS): (a), (b) and (c) are 6.25% S vacancies in 2H, 1T and 1T′ phase, (d) and (e) are 11.11% S vacancy in 2H and 1T phase respectively. Green and red vertical bars indicate the energy window considered for Integrated Local Density of States (ILDOS). Images on the right of each plot are ILDOS showing localization of the highlighted states. Grey spheres represent Mo atoms. Yellow and green spheres represent S atoms in top and bottom layers respectively.

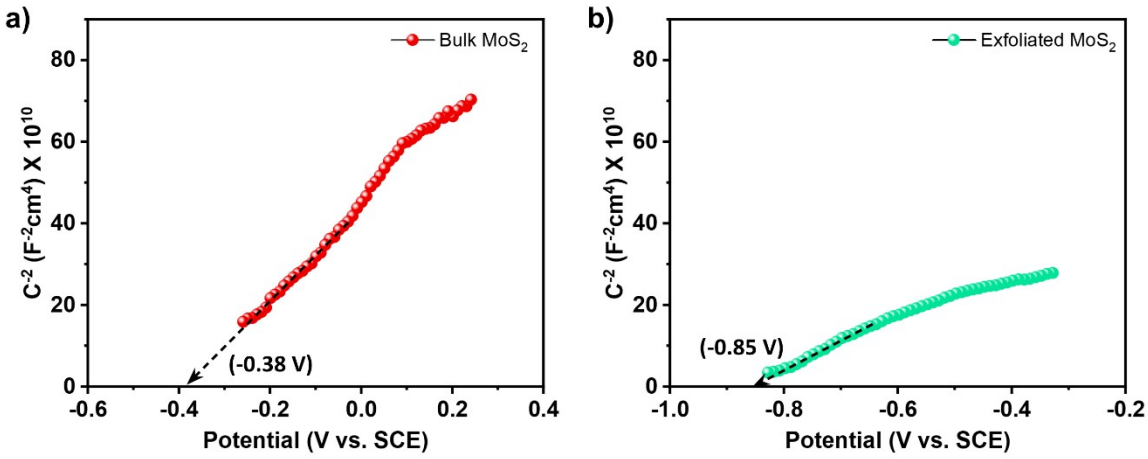

Figure S13. Mott–Schottky plots of interfacial capacitance derived from EIS data for a) bulk and b) exfoliated MoS_2 at 1000 Hz in 0.1 M Na_2SO_4.

We have also calculated the carrier density from the Mott-Schottky (M-S) plot. The capacitance measurements are presented as an M-S plot following the equation below (Mott-Schottky equation)[26]-

$$1/C^2 = \frac{2}{N_A \varepsilon_0 \varepsilon e}(E - E_{fb} - \frac{kT}{e})$$

Where, C is the interfacial capacitance (i.e., capacitance of the semiconductor depletion layer), ε is the dielectric constant of the material, ε_0 is the permittivity of free space (8.85×10^{-12} Fm^{-1}), N_A is the carrier density (cm^{-3}) in the semiconductor, E is the applied potential, E_{fb} is the flat band potential, T is the absolute temperature (298 K), k is the Boltzmann constant (1.38×10^{-23} JK^{-1}) and e is the electron charge (1.6×10^{-19} C). ε, the relative permittivity of MoS_2 is assumed here to be 5.35.[27] Putting these values in the above equation, the carrier density (N_A) as calculated from the slope of the MS plot is found to be 2.3×10^{15} cm^{-3} for bulk MoS_2 and 3.55×10^{15} cm^{-3} for exfoliated MoS_2. The increased carrier density of exfoliated MoS_2 suggests better charge conductivity and in turn increased metallic property of the exfoliated sample.

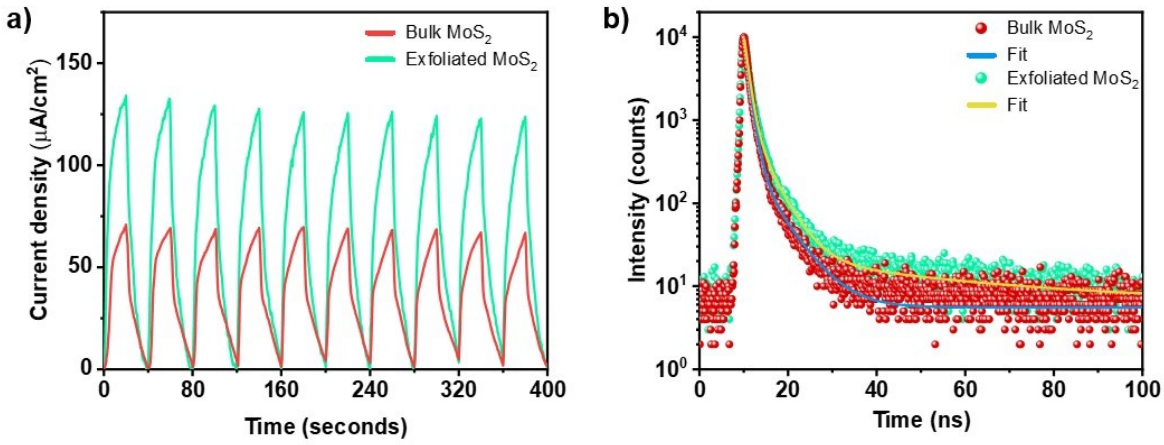

Figure S14. a) Transient photocurrent response of bulk and exfoliated MoS_2 at a bias voltage of 0.5 V vs. SCE (Saturated Calomel Electrode). b) Time-resolved photoluminescence measurements of the bulk and exfoliated MoS_2 (excitation wavelength 405 nm).

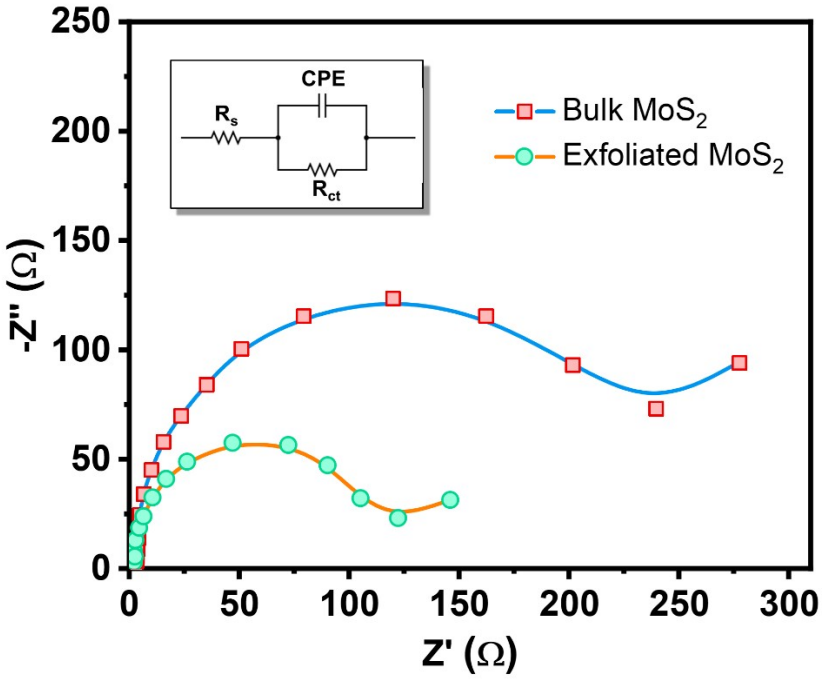

Figure S15. Electrochemical impedance spectra of bulk and exfoliated MoS_2 in 0.1 M K_2SO_4 solution. R_{ct} is calculated from the radius of the half circle.

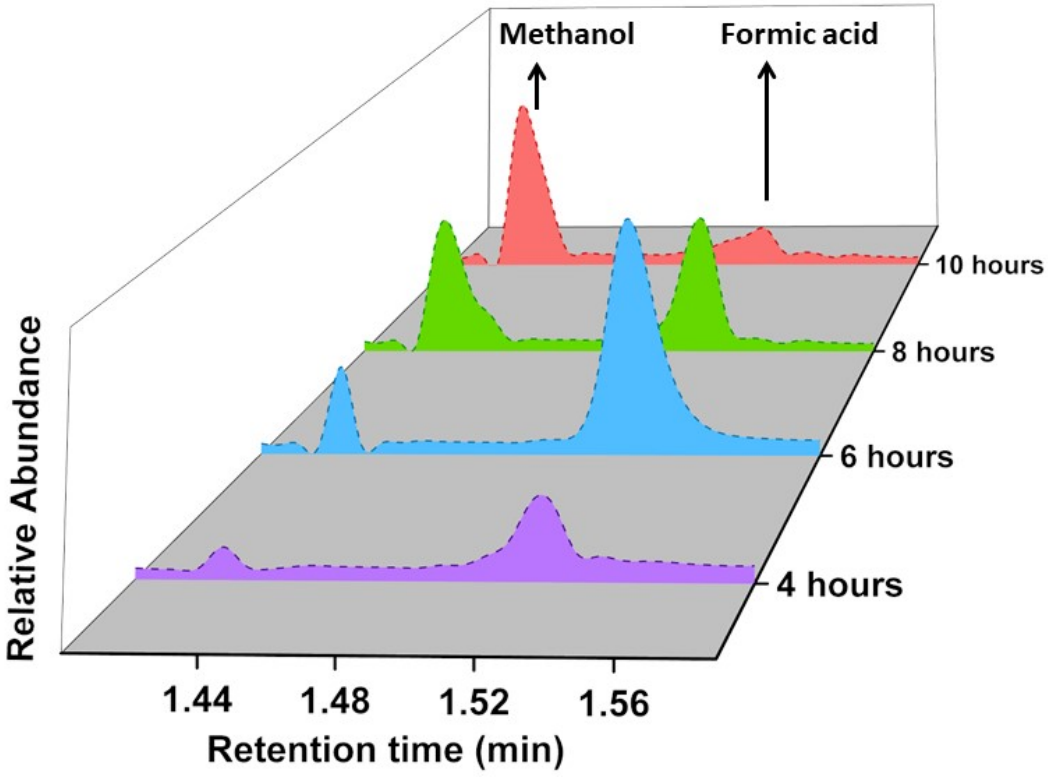

Figure S16. Time-dependent GC-MS spectra of the reaction mixture.

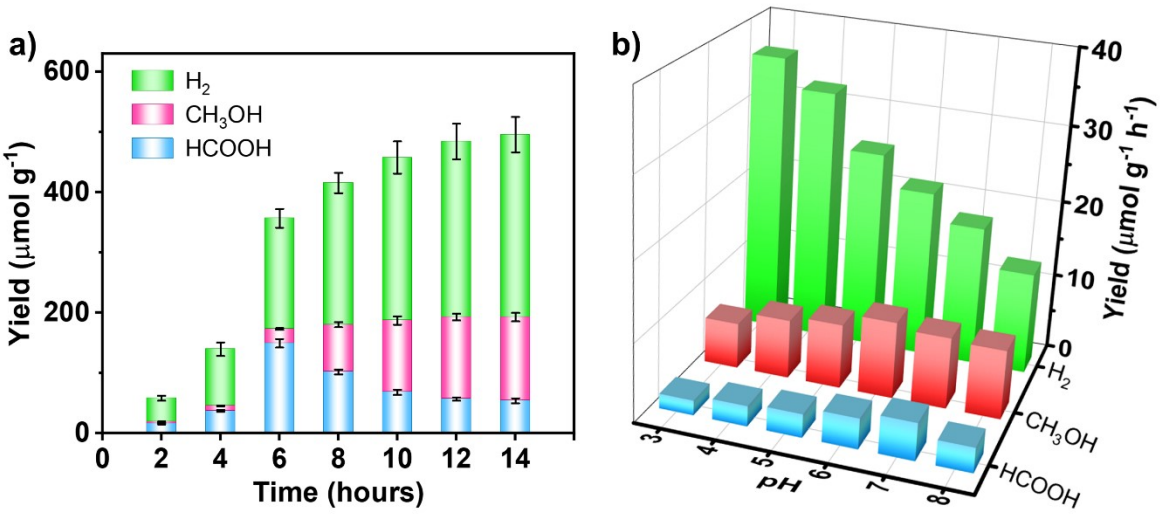

Figure S17. a) Time-dependent and b) pH-dependent photocatalytic HER (hydrogen evolution reaction) in addition to the CO_2 reduction reaction. HER is the competitive reaction during the CO_2 reduction reaction.

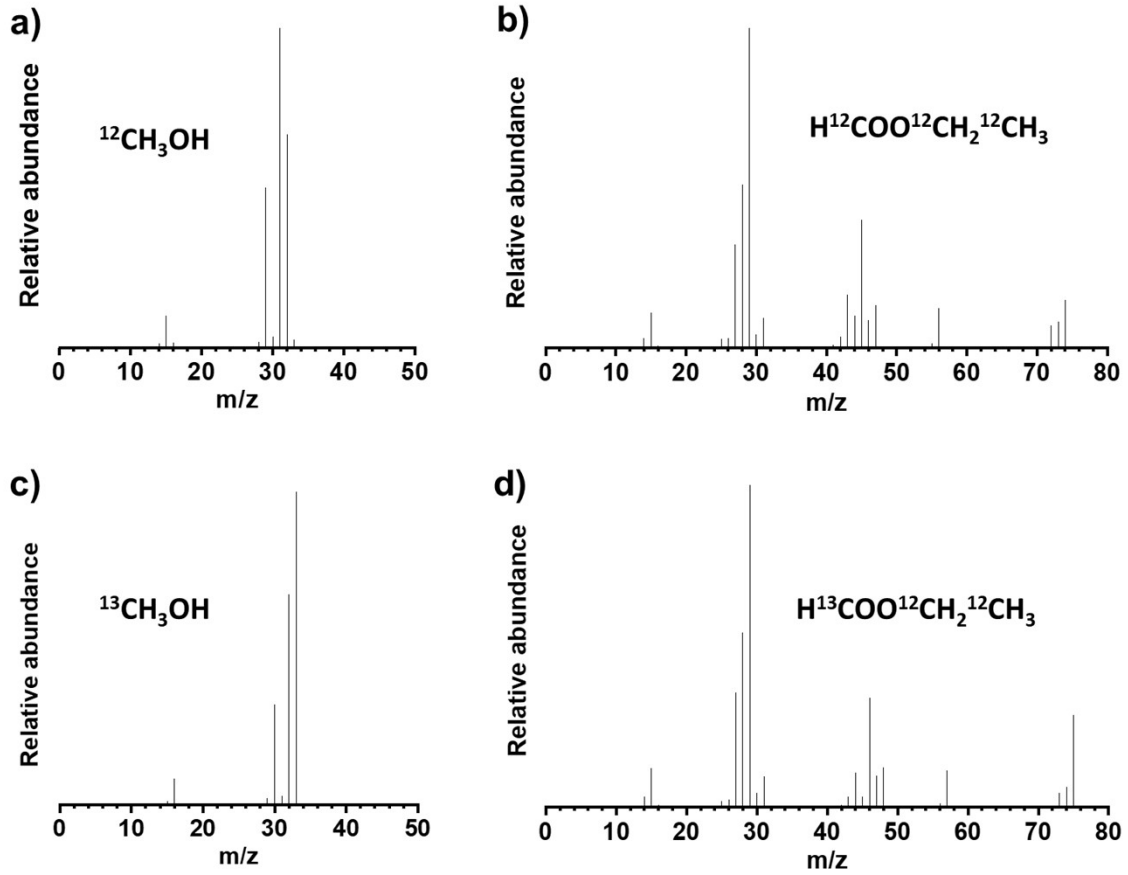

Figure S18. a) and b) GC-MS spectra of methanol and ethyl formate after photocatalytic reduction of $^{12}CO_2$ respectively. c) and d) GC-MS spectra of methanol and ethyl formate after photocatalytic reduction of $^{13}CO_2$ respectively.

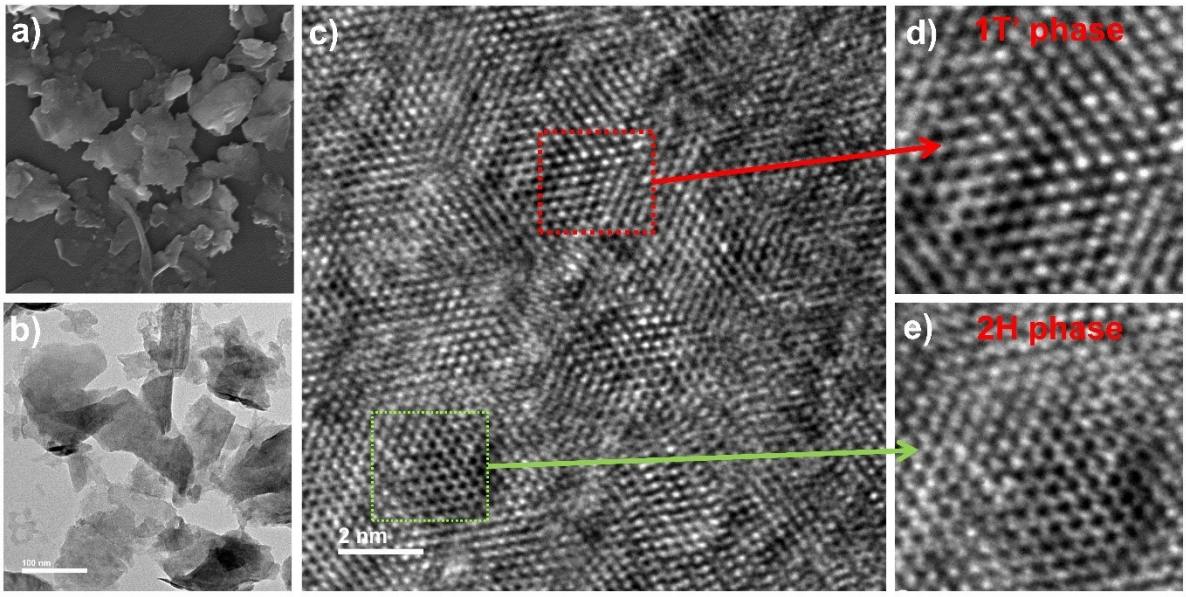

Figure S19. a) SEM and b) TEM image of the recovered exfoliated MoS_2. c) HRTEM image of the recovered exfoliated MoS_2 catalyst showing the presence of d) 1T′ phase and e) 2H phase.

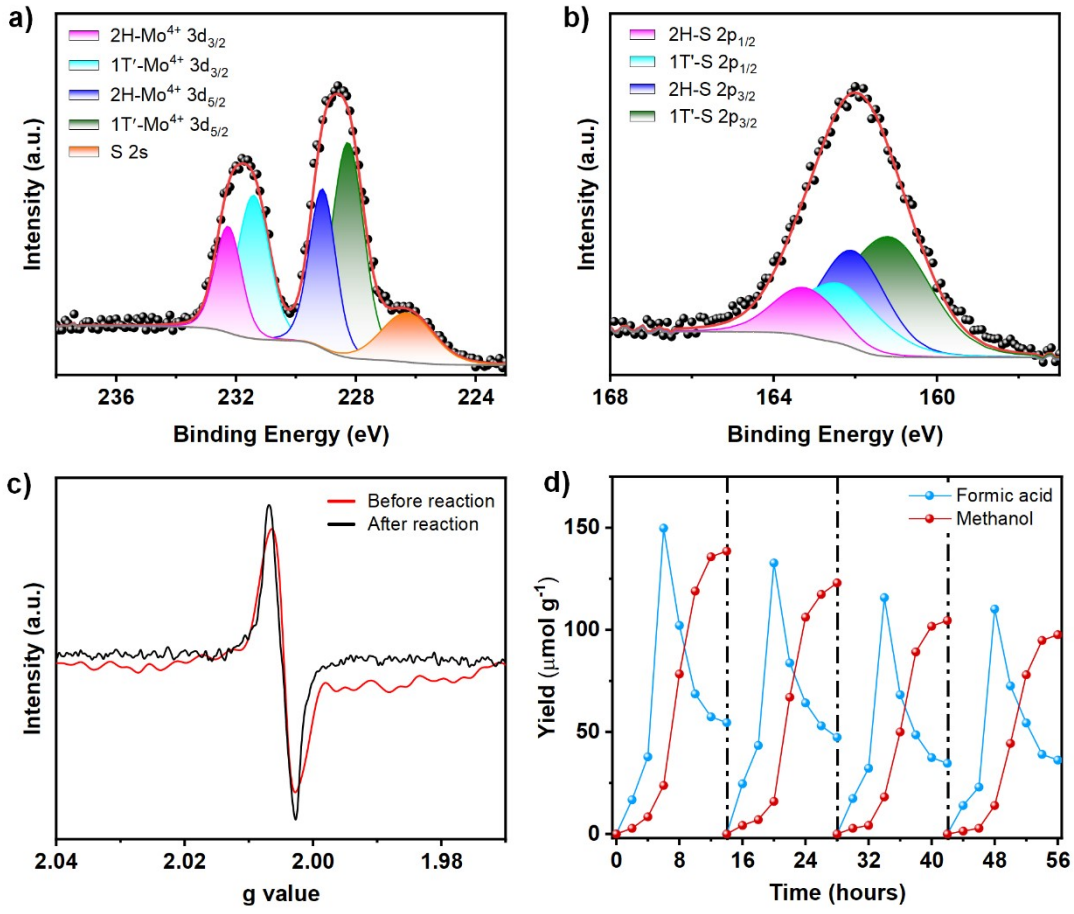

Figure S20. a) Mo 3d and b) S 2p XPS analysis showing the presence of 2H phase and 1T′ phase in the recovered exfoliated MoS_2. c) EPR spectra of recovered exfoliated MoS_2 catalyst have slightly lower intensity compared to before reaction catalyst. d) Catalyst recycle tests show that although the CO_2 reduction was performed by the recovered catalyst, the performance decreased in the subsequent cycles.

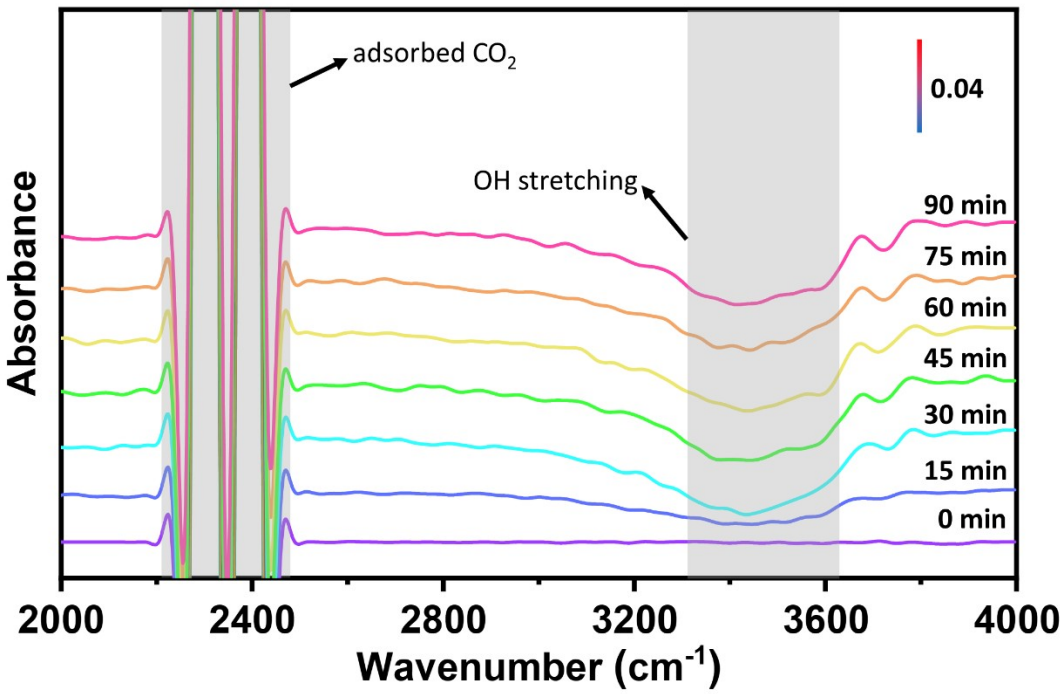

Figure S21. *In situ* FTIR spectra for coadsorption of a mixture of CO_2 and H_2O vapour on the exfoliated MoS_2 for the detection of intermediate species (2000 cm^{-1} – 4000 cm^{-1}).

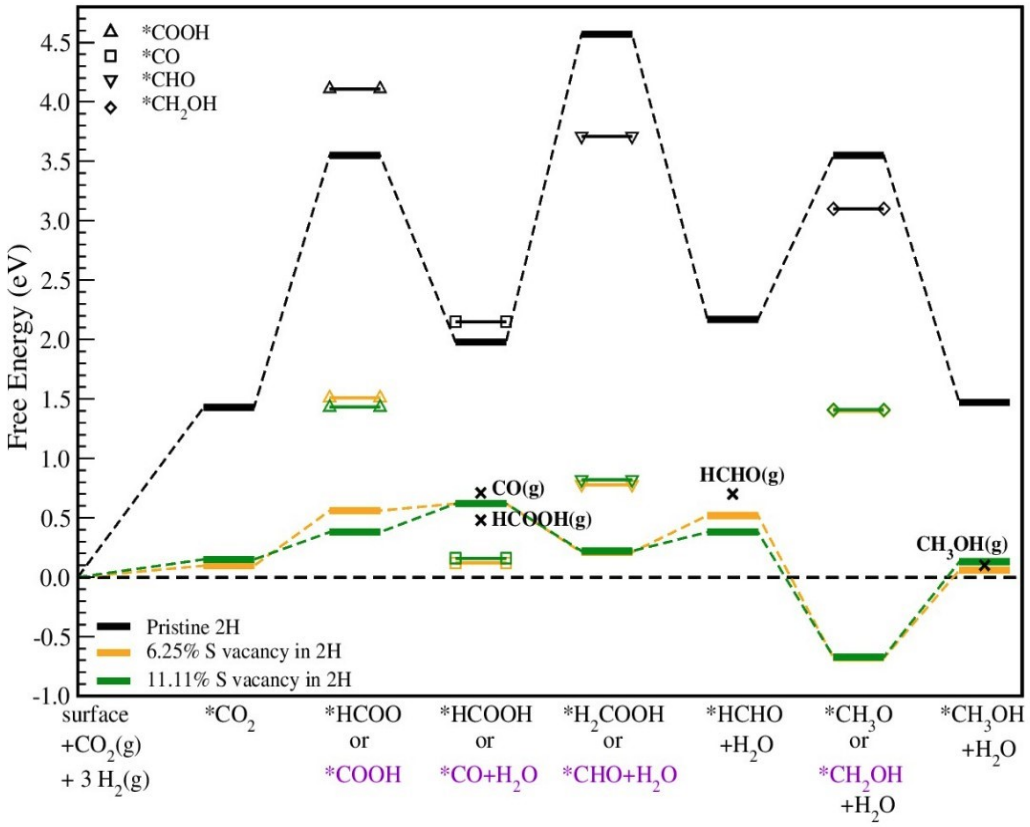

Figure S22. Free energy diagram for CO_2 reduction to CH_3OH on 2H monolayers. Thick and thin solid bars indicate the free energies of possible intermediates in each step. Black and violet species on reaction coordinate are the possible intermediates in HCOO (black) and COOH (violet) pathways. Dotted lines highlight the most favourable pathway. **x** represents free energies of stable gas phase intermediates in desorbed state. Superscript * indicates adsorbed species on the surface.

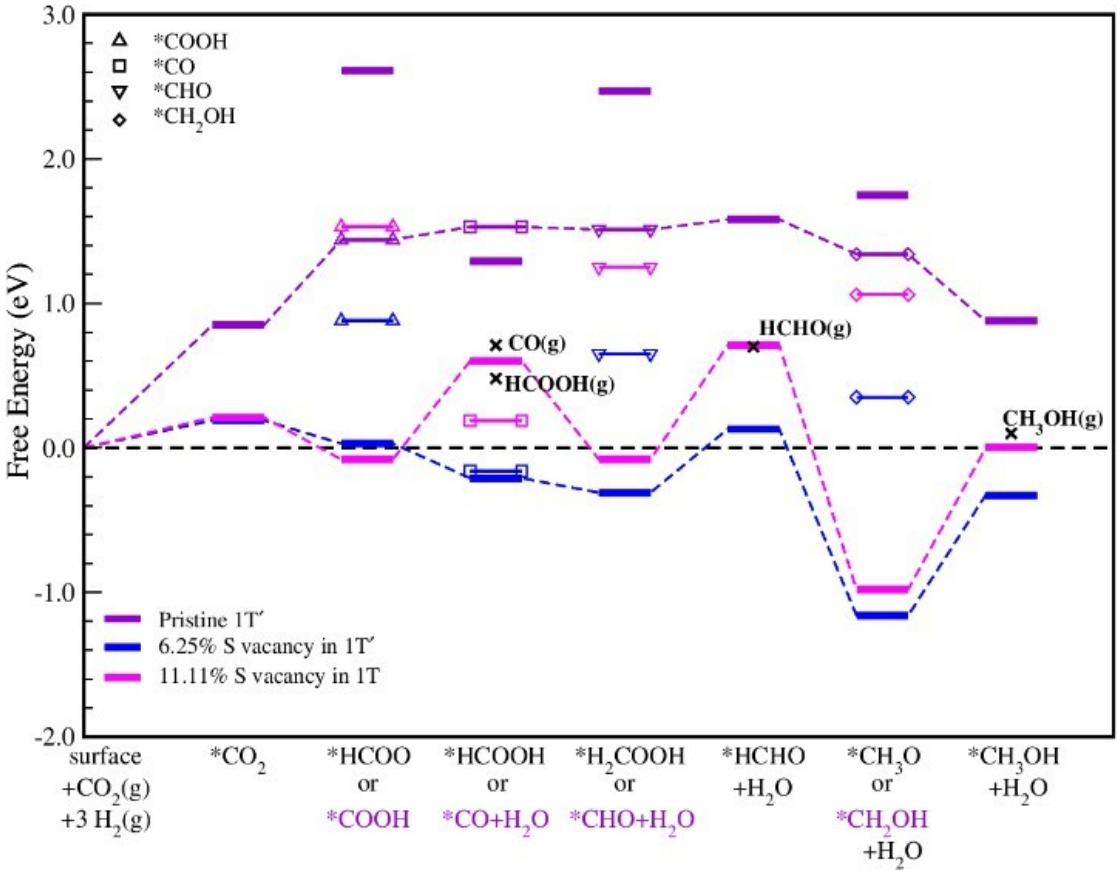

Figure S23. Free energy diagram for CO_2 reduction to CH_3OH on 1T/1T′ monolayers. Thick and thin solid bars indicate the free energies of possible intermediates in each step. Black and violet species on reaction coordinate are the possible intermediates in HCOO (black) and COOH (violet) pathways. Dotted lines highlight the most favourable pathway. **x** represents free energies of stable gas phase intermediates in desorbed state. Superscript * indicates adsorbed species on the surface.

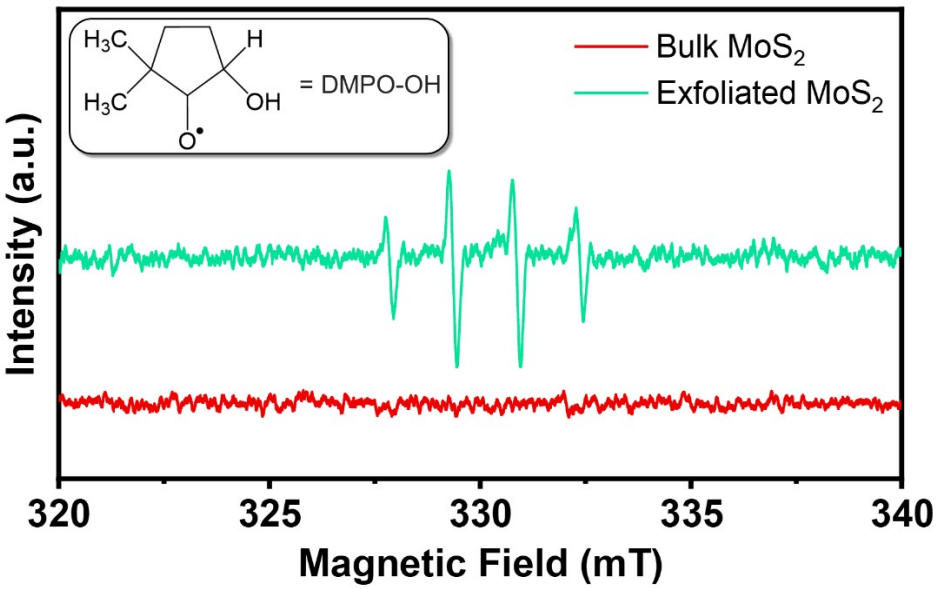

Figure S24. EPR spectra of DMPO-OH adduct from the photocatalytic water oxidation by MoS_2 nanosheets.

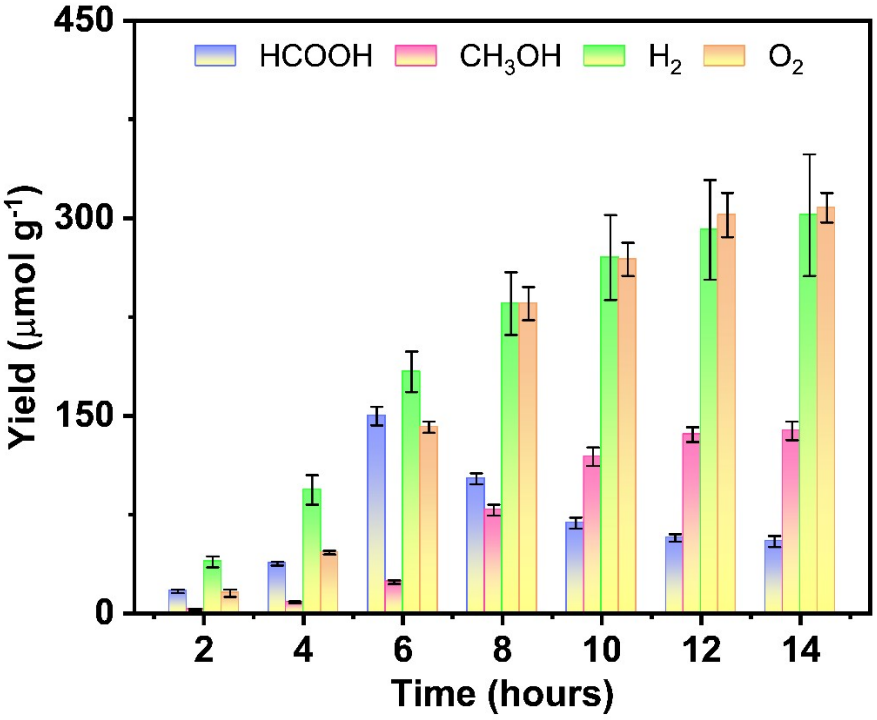

Figure S25. Yield of oxygen measured during the visible light photoreaction of CO_2.

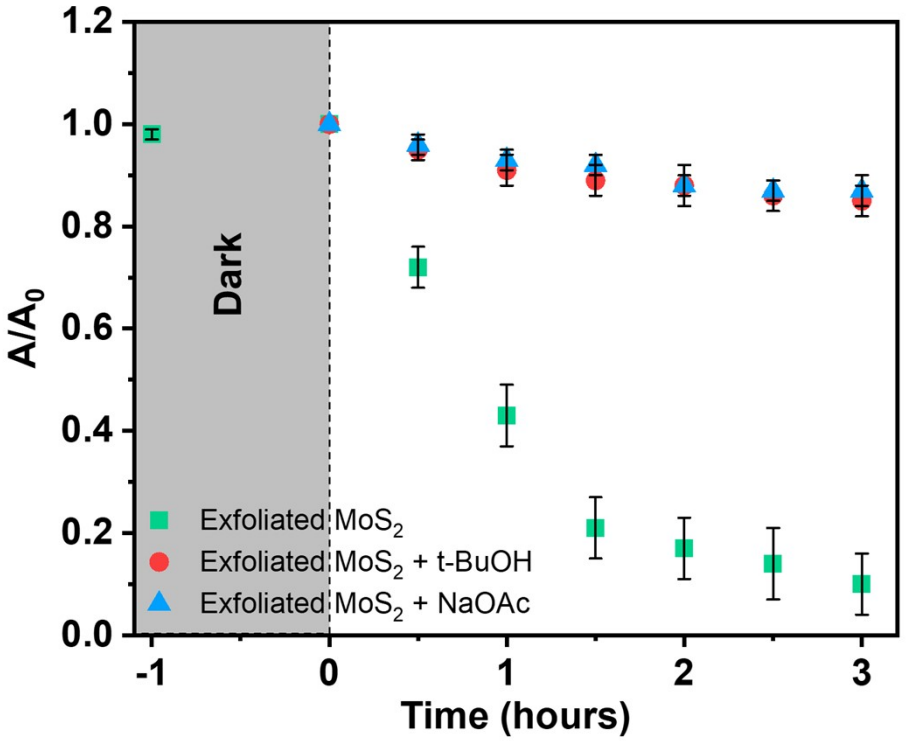

Figure S26. Photodegradation of methylene blue as a function of time in presence of exfoliated MoS_2 nanosheet.

References:

1. M. Wu, C. Liu, R. Sun, T. Yu, Y. Li and G. Yang, *Int. J. Energy Res.,* 2020, **44**, 4605.
2. P. Giannozzi, S. Baroni, N. Bonini, M. Calandra, R. Car, C. Cavazzoni, D. Ceresoli, G. L. Chiarotti, M. Cococcioni and I. Dabo, *Journal of physics: Condensed matter,* 2009, **21**, 395502.
3. J. P. Perdew, K. Burke and M. Ernzerhof, *Phys. Rev. Lett.,*1996,**77**,3865.
4. D. Vanderbilt, *Phys. Rev. B,* 1990, **41**, 7892.
5. H. J. Monkhorst and J. D. Pack, *Phys. Rev. B,* 1976**, 13**, 5188.
6. S. Baroni, P. Giannozzi and A. Testa, *Phys. Rev. Lett.*, 1987, **58** ,1861.
7. S. Baroni, S. de Gironcoli, D. A. Corso and P. Giannozzi, *Rev. Mod. Phys.*, 2001, **73**, 515.
8. X. Gonze, *Phys. Rev. A*, 1995, 52,1096.
9. J. K. Nørskov, J. Rossmeisl, A. Logadottir, L. Lindqvist, J. R. Kitchin, T. Bligaard and H. Jonsson, *The Journal of Physical Chemistry B,* 2004**, 108**, 17886.
10. Bendavid L. I. and Carter E. A., *J. Phys. Chem. C*, 2013, **117**, 26048.
11. Tang Q. and De-en Jiang., *ACS Catalysis*, 2016, **6**,4953.
12. Maya Bar-Sadan, Datar A. And Ramasubramaniam A., *J. Phys. Chem. C*, 2020, **124**, 20116.
13. Kan M., Wang J., Li X., Zhang S., Li Y., Kawazoe Y., Sun Q. and Jena P., *J. Phys. Chem. C,* 2014, **118,** 1515.
14. Rui Li, Ting Hu and Dong J., *J. Chem. Phys.*, 2013, **139**, 174702.
15. Mak K. F., Lee C., Hone J., Shan J. and Heinz T. F., *Phys. Rev. Lett.*, 2010, **105**, 136805.
16. Yu Y., Nam G. H., He Q. et al., *Nature Chem,* 2018*,* **10**, 638.
17. W. Tu, Y. Li, L. Kuai, Y. Zhou, Q. Xu, H. Li, X. Wang, M. Xiao and Z. Zou, *Nanoscale*, 2017, **9**, 9065-9070.
18. Y. Zhao, W. Cai, Y. Shi, J. Tang, Y. Gong, M. Chen and Q. Zhong, *ACS Sustainable Chem. Eng.*, 2020, **8**, 12603-12611.
19. W. Dai, J. Yu, Y. Deng, X. Hu, T. Wang and X. Luo, *Appl. Surf. Sci.*, 2017, **403**, 230-239.
20. J. Lu, Z. Zhang, L. Cheng and H. Liu, *New Journal of Chemistry*, 2020, **44**, 13728-13737.
21. Y. Zheng, X. Yin, Y. Jiang, J. Bai, Y. Tang, Y. Shen and M. Zhang, *Energy Technology*, 2019, **7**, 1900582.
22. F. Xu, B. Zhu, B. Cheng, J. Yu and J. Xu, *Advanced Optical Materials*, 2018, **6**, 1800911.
23. R. A. Geioushy, I. M. Hegazy, S. M. El-Sheikh and O. A. Fouad, *Journal of Environmental Chemical Engineering*, 2022, **10**, 107337.
24. H. Qin, R.-T. Guo, X.-Y. Liu, W.-G. Pan, Z.-Y. Wang, X. Shi, J.-Y. Tang and C.-Y. Huang, *Dalton Trans.*, 2018, **47**, 15155-15163.
25. R. Kim, J. Kim, J. Y. Do, M. W. Seo and M. Kang, *Catalysts*, 2019, **9**, 998.
26. F. Caballero-Briones, J. M. Artés, I. Díez-Pérez, P. Gorostiza and F. Sanz, *J. Phys. Chem. C*, 2009, **113**, 1028-1036.
27. Y. Hou, G. Wang, C. Ma, Z. Feng, Y. Chen and T. Filleter, *Materials Characterization*, 2022, **193**, 112313.